Dye-sensitized photoelectrochemical water oxidation through a buried junction

Pengtao Xu[a,b,c,1], Tian Huang[a,b,c,d,e,1], Jianbin Huang[d], Yun Yan[d,2], and Thomas E. Mallouk[a,b,c,2]

[a]Department of Chemistry, The Pennsylvania State University, University Park, PA 16802; [b]Department of Biochemistry and Molecular Biology, The Pennsylvania State University, University Park, PA 16802; [c]Department of Physics, The Pennsylvania State University, University Park, PA 16802; [d]Beijing National Laboratory for Molecular Science, College of Chemistry and Molecular Engineering, Peking University, 100871 Beijing, China; and [e]Academy for Advanced Interdisciplinary Studies, Peking University, 100871 Beijing, China

Water oxidation has long been a challenge in artificial photosynthetic devices that convert solar energy into fuels. Water-splitting dye-sensitized photoelectrochemical cells (WS-DSPECs) provide a modular approach for integrating light-harvesting molecules with water-oxidation catalysts on metal-oxide electrodes. Despite recent progress in improving the efficiency of these devices by introducing good molecular water-oxidation catalysts, WS-DSPECs have poor stability, owing to the oxidation of molecular components at very positive electrode potentials. Here we demonstrate that a solid-state dye-sensitized solar cell (ss-DSSC) can be used as a buried junction for stable photoelectrochemical water splitting. A thin protecting layer of TiO_2 grown by atomic layer deposition (ALD) stabilizes the operation of the photoanode in aqueous solution, although as a solar cell there is a performance loss due to increased series resistance after the coating. With an electrodeposited iridium oxide layer, a photocurrent density of 1.43 mA cm^{-2} was observed in 0.1 M pH 6.7 phosphate solution at 1.23 V versus reversible hydrogen electrode, with good stability over 1 h. We measured an incident photon-to-current efficiency of 22% at 540 nm and a Faradaic efficiency of 43% for oxygen evolution. While the potential profile of the catalyst layer suggested otherwise, we confirmed the formation of a buried junction in the as-prepared photoelectrode. The buried junction design of ss-DSSs adds to our understanding of semiconductor–electrocatalyst junction behaviors in the presence of a poor semiconducting material.

water oxidation | dye-sensitized photoelectrochemical cell | solid-state dye-sensitized solar cell | artificial photosynthesis | dual working electrode

Artificial photosynthesis mimics the natural processes of converting solar energy, water, and CO_2 into chemical fuels. One of the key steps involved in artificial photosynthesis is water oxidation, in which an oxygen molecule is generated by the four-electron oxidation of two water molecules. This process is kinetically demanding and occurs at positive potentials where undesired side reactions lead to the oxidation of molecular components in both artificial and natural photosynthetic systems.

Water-splitting dye-sensitized photoelectrochemical cells (WS-DSPECs) are artificial photosynthetic devices that exemplify this problem (1, 2). In the WS-DSPEC, a high surface area electrode based on a metal oxide, typically a mesoporous TiO_2 or SnO_2 film that is several micrometers thick, adsorbs a monolayer of dye molecules for light harvesting. Coupling these dye molecules with water-oxidation catalysts enables light-driven water oxidation in a manner analogous to Photosystem II. Although early versions of these cells were inefficient (3), the introduction of molecular water-oxidation catalysts (4) and the use of core–shell electrode architectures has significantly improved the quantum yield for water splitting (5–7). However, despite these improvements WS-DSPECs generally suffer from poor stability, with substantial photocurrent decay within minutes. The problem is primarily due to dye and catalyst decomposition and desorption (8, 9). When in contact with water, the anchoring groups of the dye and catalyst molecules attached to the metal-oxide surface (typically phosphonate groups)

are susceptible to both oxidation and hydrolysis (10, 11). Dye desorption is accelerated at elevated pH (pH > 5). Increasing the pH also lowers the electron injection yield, because the conduction band edge potential of the metal oxide shifts in the cathodic direction by about 60 mV per pH unit (12), making electron transfer from the photoexcited dye to the metal oxide less favorable. The water-oxidation reaction, however, is more thermodynamically favorable at higher pH. Operating WS-DSPECs in a more basic environment can produce more photocurrent if molecular desorption is suppressed and a high electron injection yield is maintained at the same time. This can be achieved, in principle, by decoupling the light absorption and water-oxidation reactions in WS-DSPECs, so that each process take places in a favorable local environment.

One strategy for overcoming these difficulties is to create a "mummy" electrode architecture in which the sensitizer molecules are encapsulated by a nanometer-thick metal-oxide film prepared by atomic layer deposition (ALD) (13, 14). Although stabilized photocurrents are attained by this technique, the electron injection yield from the sensitizer to the metal oxide is significantly reduced due to concurrent charge injection into the protecting layer. An alternative approach, which we explore here, is to interpose a solid-state hole conductor between the dye and the water-oxidation catalyst. This strategy exploits the architecture of the solid-state dye-sensitized solar cell (ss-DSSC), which is adapted to water splitting with five key components (Fig. 1): (i) a

Significance

Artificial photosynthetic systems use molecular light absorbers to convert sunlight into useful chemical fuels such as hydrogen, methanol, or ammonia. A key bottleneck in these systems is the oxidation of water to produce O_2. This anodic reaction occurs under strongly oxidizing conditions that result in damage to organic dyes, electron relays, and catalyst molecules. Here we show that encapsulation of the molecular components of a solid-state dye-sensitized solar cell by a 2-nm-thick coating of TiO_2 dramatically improves cell stability under water-splitting conditions. The physical separation of the dye from the solution in which the water-splitting reaction takes place enables the use of dyes that efficiently absorb in the visible and allows optimization of the pH of catalytic water oxidation.
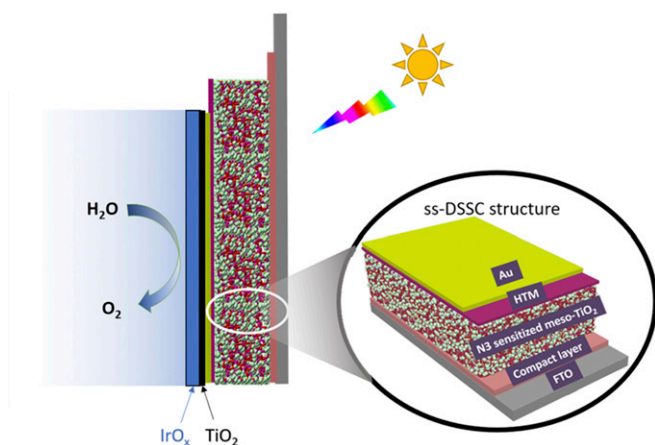
CHEMISTRY

Fig. 1. ss-DSSC as a buried junction for visible-light photoelectrochemical water oxidation.

transparent conductive substrate, (*ii*) a mesoporous metal-oxide thin film, (*iii*) a monolayer of sensitizer molecules, (*iv*) a solid-state hole-transport material, and (*v*) a top metal contact (15). ss-DSSCs of high efficiency and high stability have been reported (16). However, the ss-DSSC is intrinsically vulnerable to water because the spin-coated hole-transport layer and the deposited top contact are not pinhole-free and are water permeable (17). Oxidized hole-transport molecules may also dissolve in water. These problems can be resolved by using an ALD-grown metal oxide as a conformal coating over the photoanode, a technique that has been widely used to improve the stability of semiconductor photoanodes in harsh environments (18). For example, in either strongly acid or basic environments, Si photoanodes protected by ALD-TiO$_2$ films can operate stably under water oxidation conditions for at least 8 h, whereas the same photoelectrodes without the TiO$_2$ layer quickly fail (19).

Here we explore the adaptation of the ss-DSSC as a buried photovoltaic (PV) junction for use in WS-DSPECs. (Fig. 2) We used ALD to coat a 2-nm-thin layer of TiO$_2$ on the top contact (Au) to protect the ss-DSSC against oxidation and hydrolysis reactions in water. Although the ALD coating introduces series resistance that lowers the photocurrent in air, ss-DSSCs show enhanced stability in contact with the aqueous environment. We further electrodeposited an iridium oxide film on the Au layer as a water-oxidation catalyst. The as-prepared electrode yields relatively high photocurrent and good stability toward water oxidation. Using the Au contact of the ss-DSSCs as a second working electrode, we are able to monitor the potential drop across the catalyst layer. We find that the as-prepared electrode functions as a buried junction, because under conditions of water oxidation, the buried ss-DSSC shows the same current–voltage profile as the corresponding two-electrode PV cell. Using this buried junction strategy, we make water oxidation possible with N3 dye molecules, which possess a lower oxidizing potential than commonly used phosphonate-based Ru polypyridyl sensitizers. This demonstrates that dye molecules with unfavorable redox properties toward water oxidation can be effectively utilized in buried junction WS-DSPECs.

Experimental

ss-DSSC Fabrication. FTO substrates (fluorine-doped SnO$_2$-coated glass, 8 Ω/cm^2; Hartford Glass) were etched with zinc powder and HCl (2 M) to prepare the desired patterns for photoelectrodes. The FTO-coated glass was then cleaned sequentially by sonication in soapy water, ethanol, and distilled water, followed by 10-min UV-ozone treatment. A compact layer of TiO$_2$ was deposited onto the FTO surface by spin-coating at a speed of 500 rpm for 30 s with a solution of titanium butoxide (≥97.0%, Fluka) diluted in 2-butanol (1:30 vol/vol). Films were sintered at 500 °C for 30 min.

After cooling to room temperature, a mesoporous TiO$_2$ film was doctor-bladed onto the compact layer by using a 20-nm TiO$_2$ nanoparticle paste prepared by a previously reported method (20). The electrode films were then sintered at 300 °C for 20 min, 350 °C for 10 min, and 500 °C for 30 min. The films were further treated with 50 mM aqueous TiCl$_4$ solution for 40 min at 70 °C and sintered at 500 °C again for 30 min. After cooling to 70 °C, the films were immersed in an ethanol solution containing 0.1 mM N3 dye (95%; Sigma-Aldrich) for 18 h. After dye adsorption, the films were rinsed with ethanol. Subsequently, a hole-transport layer consisting of spiro-OMeTAD ($N^2,N^2,N^{2'},N^{2'},N^7,N^7,N^{7'},N^{7'}$-octakis(4-methoxyphenyl)-9,9'-spirobi[9H-fluorene]-2,2',7,7'-tetramine) was deposited onto the dye-sensitized films. The spiro-OMeTAD solution was prepared by dissolving 130 mg of spiro-OMeTAD (99%; Aldrich) in 1 mL chlorobenzene (99.8%; Sigma-Aldrich), together with additives including 20 μL of 4-tert-butylpyridine (96%; Aldrich) and 40 μL of a 170 mM lithium bis(trifluoromethane)sulfonamide (Li-TFSI, 99.95%; Aldrich) stock solution in acetonitrile. The as-prepared solutions were filtered through a syringe filter with a pore size of 0.22 μm to remove undissolved particles before use. Spiro-OMeTAD solution (20 μL) was applied to each electrode under ambient conditions and the samples were left to dry for 1 min before spin-coating at 2,000 rpm for 30 s. Finally, a 100 nm thick Au was deposited onto the spiro-OMeTAD layer in an electron-beam evaporator (Kurt J. Lesker Lab-18), forming the complete solid-state PV device. For the fabrication of cells for use in contact with water, a 2-nm-thick TiO$_2$ film was deposited onto the gold surface at 75 °C by ALD (Cambridge Savannah 200) with tetrakis(dimethylamino)titanium(IV) (99% Strem Chemicals) as the Ti precursor. The growth rate of the TiO$_2$ film under these conditions was 0.8 Å per cycle, as determined by ellipsometry on Si wafers.

Electrodeposition of Iridium Oxide Films. A hydroxyiridate monomer solution was synthesized by alkaline hydrolysis of K$_2$IrO$_6$, as described in our previous papers (21, 22). Using the Au layer of the ss-DSSC as the working electrode, we deposited hydrous iridium oxide thin films on the Au surface from 0.4 mM hydroxyiridate(III/IV) solutions at an applied potential of 1.2 V versus Ag/AgCl (3 M NaCl) for 400 s. A home-built mechanical stirrer was used during the electrodeposition process. The thickness of the deposited film was characterized by a field-emission scanning electron microscope (Zeiss Sigma) to be about 75 nm.

Photoelectrochemical Measurements. The light source for simulating sunlight was a 150-W xenon lamp equipped with a 410-nm long-pass filter and an AM1.5 filter. The intensity of the light incident on the FTO side of the cells was 100 mW cm^{-2}, as measured by a power probe (Molectron, PM3). The effective area of each cell was 0.54 cm^2 (0.6 × 0.9 cm^2). All photoelectrochemical data were recorded on a digital potentiostat (PGSTAT128N, Autolab). The photocurrent measurements in three-electrode configuration were performed in a glass cell (96G20; FireflySci) with a Pt wire as the counter electrode and Ag/AgCl (3 M NaCl) as the reference electrode. The counter electrode was located in a separate compartment. The electrolyte was 0.1 M potassium phosphate buffer solution (pH 6.7) with 0.1 M NaClO$_4$ added as the supporting electrolyte. Before each measurement, the electrolyte was deaerated by purging with
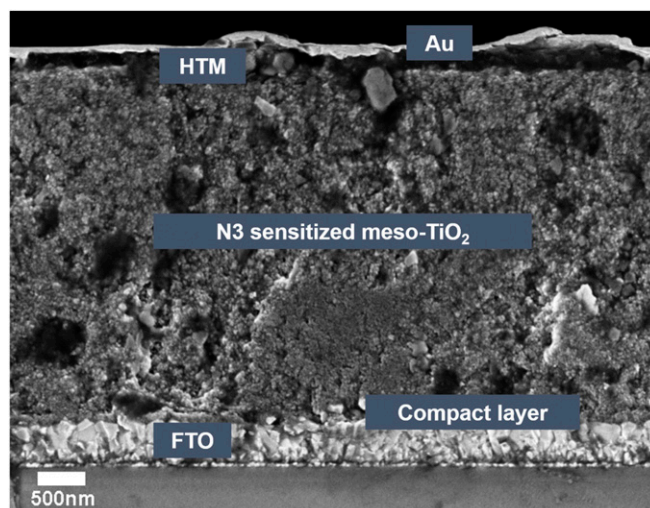

Fig. 2. Cross-sectional SEM image of an as-prepared ss-DSSC.

argon for 20 min. Electrochemical impedance measurements (EIS) were performed in galvanostatic mode. A sinusoidal current was applied at an amplitude of 5 μA over a frequency range of 10^6 to 5 Hz. All EIS measurements were carried out under open-circuit conditions under illumination of a 470-nm LED light at an intensity of 11 mW cm^{-2}. Incident photon-to-current conversion efficiency (IPCE) spectra were collected with a 500-W xenon lamp and a monochromator (Spectral Products CM110). The data were taken in 10-nm increments and the light intensity at each wavelength was measured by a Si photodiode (S130C; Thorlabs). Photocurrent data were recorded at 0.62 V vs. Ag/AgCl using the same three-electrode setup described above.

Generator–Collector O$_2$ Detection. A generator–collector method was used for O$_2$ detection as described elsewhere (23). Briefly, experiments were performed in bipotentiostat mode with two working electrodes: a Pt wire as the counter electrode and a Ag/AgCl electrode as the reference electrode. One working electrode (the generator) was the FTO contact of the photoanode; the other one (the collector) was a planar Pt electrode made by sputtering a 50-nm-thick Pt film onto an FTO glass substrate (with an adhesion layer of 5-nm Ti). The collector was masked with Kapton tape to create an active area of about 1.5 cm^2. The generator–collector electrode pair was assembled by placing the two working electrodes face-to-face with the iridium oxide layer facing the Pt electrode. A piece of a 1 mm-thick glass slide was inserted between the lateral edges as a spacer and a plastic paraffin film was wrapped around the long side of the two electrodes. The space between the two working electrodes was filled with electrolyte by capillary action when the assembly was placed in solution. A 470-nm LED light of 19.4 mW cm^{-2} was used as the light source. To measure the Faradaic efficiency for O$_2$ production, the generator and collector were held at 0.62 V and −0.3V vs. Ag/AgCl, respectively. The charge passing through the generator under illumination was compared with the total charge through the collector electrode. The Faradaic efficiency was calculated by comparison with the collection efficiency determined in the same fashion using an iridium oxide-deposited FTO as the generator, held at 1.12 V vs. Ag/AgCl, which was assumed to have a Faradaic efficiency of unity. The experiment was performed in 0.1 M phosphate buffer at pH 6.7 with 0.1 M NaClO$_4$. In some of our previously reported generator–collector measurements (24), the collector appeared to respond instantaneously upon generation of photocurrent, showing a current mirroring effect in the current–time profile. We note that this is an artifact due to the capacitive interference between the generator and collector electrodes, which can be minimized by increasing the ionic strength of the electrolyte, as pointed out by Sherman et al. (23) When measurements are made at sufficiently high electrolyte concentration, the time lag in the collector current reflects the time needed for oxygen to diffuse from the generator to the collector electrode.

Results and Discussion

Preparation of ss-DSSCs. The cross-sectional structure of an as-prepared ss-DSSC is shown in Fig. 2. The performance of the ss-DSSCs was found to increase over time after fabrication, reaching a maximum after 5 d (*SI Appendix*, Fig. S1), which can be attributed to partial air oxidation of the spiro-OMeTAD hole conductor (25). Fig. 3A (line 1) shows typical current density–voltage (J-V) curves of an ss-DSSC, and the corresponding PV properties are summarized in *SI Appendix*, Table S1. The short-circuit current density (J$_{sc}$) and open-circuit voltage (V$_{oc}$) for the ss-DSSCs are 3.29 mA cm^{-2} and 712 mV, respectively, which is comparable with other N3-sensitized solar cells (26). However, the power conversion efficiency of ss-DSSCs made in our laboratory was only 0.76% due to a low fill factor (0.32); in principle, a significant performance improvement in fill factor can be achieved by introducing p-type dopants into the hole-transport layer (27).

When the pristine ss-DSSC was soaked in an aqueous solution, the cell performance dropped dramatically, as shown in Fig. 3A (line 2). Decolorization of the ss-DSSC was observed during the measurement, which indicates that water penetrates through the Au layer and the spiro-OMeTAD layer. At pH 6.7, the carboxylate anchoring group of the N3 dye molecules easily desorbs from the TiO$_2$ surface because of hydrolysis of the carboxylate–metal-oxide linkage. Moreover, oxidized spiro-OMeTAD and Li-TFSI molecules may dissolve in the aqueous solution. To improve the stability of the ss-DSSC in an aqueous environment, we used ALD to grow a conformal 2-nm-thick coating of TiO$_2$
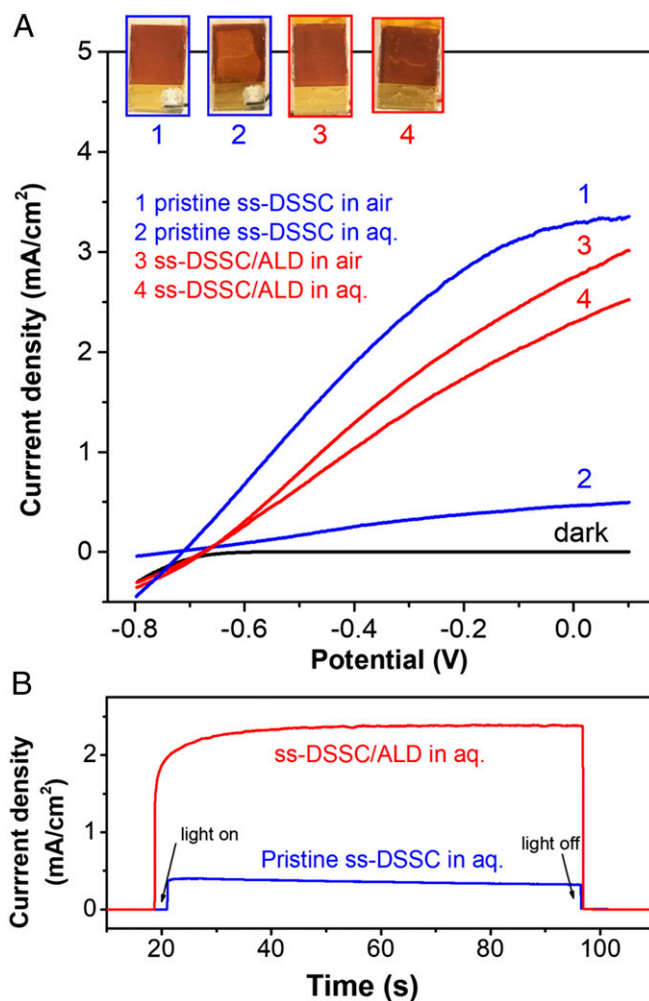

Fig. 3. Characterization of ss-DSSCs with and without ALD TiO$_2$ thin-film overlayers. (A) Two-electrode J-V curves of pristine ss-DSSC (blue) and ss-DSSC/ALD TiO$_2$ (red) electrodes in air (1, 3) and in contact with aqueous solutions (2, 4), respectively. (*Inset*) Digital images show the surface morphologies of the corresponding electrodes after testing. Scan rate: 20 mV/s. (B) Chronoamperometric measurements of pristine ss-DSSC and ss-DSSC/ALD TiO$_2$ in solution under short-circuit photoelectrochemical conditions. Light source: 100-mW cm^{-2} xenon lamp with a 410-nm long-pass filter and an AM1.5 filter.

over the exposed surface (ss-DSSC/ALD). The ss-DSSC/ALD cell shows enhanced stability in contact with an aqueous solution with slightly lower PV performance (5.6% and 16.4% drops in V$_{oc}$ and J$_{sc}$, respectively, Fig. 3A, line 3) but a steady photocurrent of 2.38 mA cm^{-2} under short-circuit conditions (Fig. 3B).

Nyquist plots derived from EIS measurements of the ss-DSSC before and after ALD coating are shown in *SI Appendix*. The series resistance of the cell increases upon heating to the temperature of the ALD cycles, and more significantly when the TiO$_2$ coating is applied. The largest resistive component can be attributed to charge-transfer resistance at the spiro-OMeTAD/TiO$_2$ interface.

Electrochemical Deposition of the IrO$_x$ Water-Oxidation Catalyst. To catalyze water oxidation, we electrochemically deposited an iridium oxide thin film on the Au layer. The Au layer in the ss-DSSC/ALD electrode was used directly as the working electrode (WE) at an applied bias of 1.2 V vs. Ag/AgCl. As water oxidation produced protons at the electrode surface, iridium oxide nanoparticles were formed in situ by acid condensation of soluble
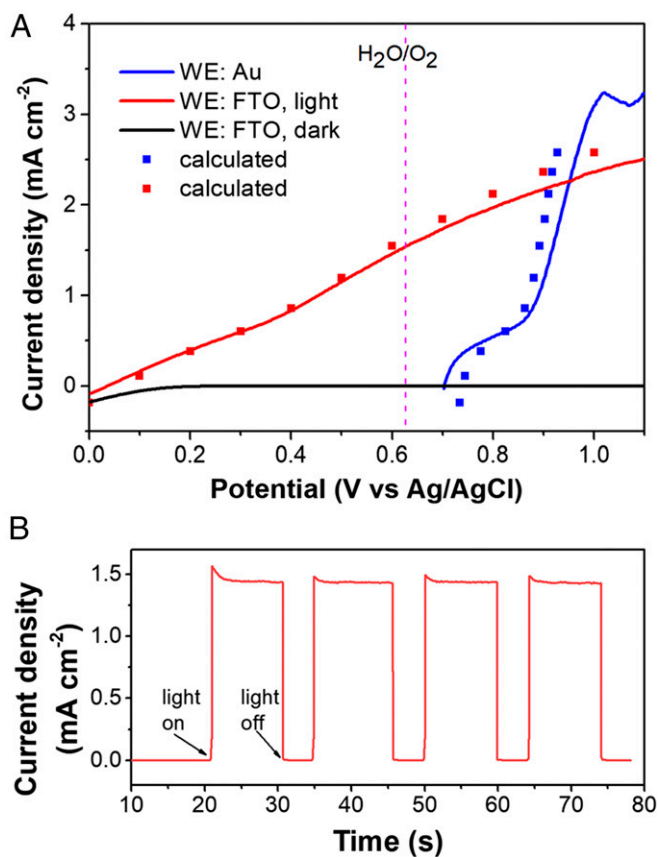
Fig. 4. Characterization of an ss-DSSC/ALD/IrO$_x$ electrode as a photoanode. (*A*) Measured (lines) and calculated (squares) linear sweep voltammetric curves of the ss-DSSC/ALD/IrO$_x$ electrode. Scan rate: 20 mV/s. (*B*) Three-electrode photocurrent measurement at an applied bias of 0.62 V vs. Ag/AgCl. Light source: 100-mW/cm^2 xenon lamp with a 410-nm long-pass filter and an AM1.5 filter.

hydroxyiridate anions (21). Consistent with previous observations, we saw an increasing current during the deposition process and the color of the electrode surface turned from gold to dark blue. We carried out the electrodeposition with a home-built mechanical stirrer operated close to the electrode surface because attempts to deposit a uniform IrO$_x$ film by this method failed when only a magnetic stir bar was used. An SEM image shows the thickness of the iridium oxide film deposited on Au to be about 76 nm (*SI Appendix*, Fig. S3). The catalyzed electrode is hereafter referred to as ss-DSSC/ALD/IrO$_x$.

The electrocatalytic performance of the deposited iridium oxide films was examined by using the Au layer as the WE. A cyclic voltammogram (*SI Appendix*, Fig. S4) shows typical redox peaks or shoulders for the Ir(IV)/Ir(III) and Ir(V)/Ir(IV) couples, and we obtained a surface coverage of 23.6 ± 2.1 nmol/cm^2 of electroactive Ir sites by integrating the Ir(V)/Ir(IV) wave. Fig. 4*A* (blue line) shows the corresponding linear sweep voltammogram (LSV). The electrode was found to be catalytically active and the overpotential required to drive water oxidation at a current density of 1 mA cm^{-2} was 0.27 V, which is comparable to reported overpotentials at the same current densities (19, 28).

Photoelectrochemical Properties of Catalyzed Photoelectrodes. Water oxidation at back-side illuminated ss-DSSC/ALD/IrO$_x$ electrodes was characterized by linear sweep voltammetry by connecting the WE lead of a three-electrode cell to the FTO back contact. As shown in Fig. 4*A* (red line), the photocurrent onset potential shifted cathodically by 0.67 V, which corresponds

to the photovoltage provided by the ss-DSSC. At the formal potential for water oxidation (0.62 V vs. Ag/AgCl), the ss-DSSC/ALD/IrO$_x$ electrode produced a steady photocurrent density of 1.43 mA cm^{-2} (Fig. 4*B*).

Lin and Boettcher (29, 30) have developed a dual-WE technique to understand the junction behavior of semiconductor–electrocatalyst (SC-EC) layers in photoelectrochemical cells. By making a direct electrical contact to the EC layer, its potential during operation can be monitored. Two types of junctions can be identified (Fig. 5*A*). One is an adaptive SC|EC junction in which the EC is electrolyte/ion permeable. In this case, the extent of band bending at the SC surface depends on the potential of redox couples in the electrolyte and its Fermi level depends on the chemical potential of the EC (V_{EC}). The other extreme is a buried junction in which the EC effectively separates the SC from the electrolyte and V_{EC} determines both the band bending
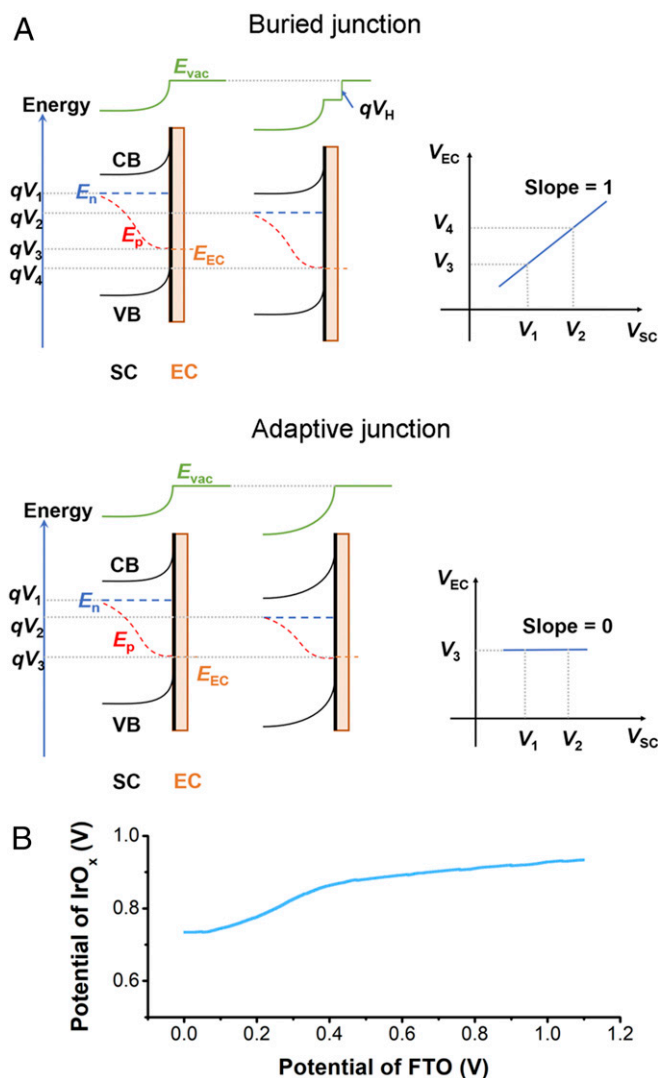

Fig. 5. (*A*, *Left*) Energy diagrams at the SC-EC interface under illumination for a buried and an adaptive junction, including the SC conduction band (CB) and valence band (VB), electron quasi-Fermi level (E_n), hole quasi-Fermi level (E_p), EC energy level (E_{EC}). (*A*, *Right*) electrocatalyst potential (V_{EC}) change as a function of the SC potential (V_{SC}). Note that the applied bias (V_1 to V_2) in a buried junction drops at the Helmholtz layer (V_H) and in an adaptive junction, the applied bias changes band bending. (*B*) Catalyst potential (V_{Au} vs. Ag/AgCl) recorded during the LSV measurement shown in Fig. 4*A* (red line) plotted against V_{FTO}.

and the Fermi level of the SC. By monitoring V_{EC} when scanning V_{SC} during LSV measurements, one would expect a linear relationship between V_{EC} and V_{SC}, with a slope of 1 or 0 for a buried junction or an adaptive junction, respectively (31).

The Au layer in ss-DSSC/ALD/IrO$_x$ serves as a natural potential probe for the IrO$_x$ catalyst layer, and the ss-DSSC in ss-DSSC/ALD/IrO$_x$ electrode resembles an SC. By measuring the voltage between the FTO and Au contacts in the ss-DSSC/ALD/IrO$_x$ electrode, we are able to monitor the catalyst potential (V_{cat}) change in situ during linear sweep voltammetry (Fig. 5B). Interestingly, the potential profile appears to indicate that the ss-DSSC/ALD/IrO$_x$ electrode is an adaptive junction because the applied potential through FTO (V_{FTO}) changes V$_{cat}$ slightly, with a slope far from the value of 1 expected for a buried junction. However, we can still categorize our electrode as a buried junction toward photoelectrochemical water oxidation, because by relating the FTO potential change in Fig. 5B to the J-V curve in Fig. 3A (line 4), we can reconstruct the LSV curves of the catalyst (Fig. 4A, blue squares) as well as that of the ss-DSSC/ALD/IrO$_x$ electrode under illumination (Fig. 4A, red squares; see *SI Appendix*, Table S2). This suggests that the ss-DSSC in ss-DSSC/ALD/IrO$_x$ electrode retains its PTV performance. The difficulty that arises in interpreting the junction behavior from Fig. 5B arises from the poor semiconducting property of the ss-DSSC. As a result of the low fill factor of the ss-DSSC, external potential changes applied to the ss-DSSC/ALD/IrO$_x$ electrode will drop more in the ss-DSSC than at the IrO$_x$–electrolyte interface so that their current densities match. For photoanodes prepared from Si solar cells with high fill factor, LSV curves under illumination are observed as shifting those measured with the corresponding catalyst layers in the anodic direction by a value close to the photovoltage of the buried solar cells (19), because a very small drop in photovoltage is adequate to supply the current passing through EC–electrolyte interface.

We tested the stability of the oxygen-evolving photoelectrodes by applying a bias of 0.62 vs. Ag/AgCl for 1 h. As shown in Fig. 6, the photocurrent is relatively stable, with 71.4% retention of the initial photocurrent at the end of the experiment. Slight discoloration of the photoelectrode was observed after the 1-h electrolysis, which suggests, although at a slower rate, that electrolyte can still penetrate into the ss-DSSC with the ALD coating. One explanation is that the pinhole-free ALD layer is disrupted by possible dynamic changes occurring at the ss-DSSC/ALD interface, as suggested by the low Faradaic efficiency described below.

A collector–generator (C-G) dual-WE method was applied to determine the Faradaic efficiency of O$_2$ production. In this experiment, oxygen produced at the generator surface diffuses steadily toward the collector electrode where it is reduced, and this produces a cathodic current in collector. By comparing the charges passed through generator (Q_G) and collector (Q_C), we can calculate the Faradaic efficiency (η) using $\eta = Q_C/(Q_G \times \eta_c) \times 100\%$, where η_c is the charge collection efficiency of C-G used to correct for diffusional losses of oxygen in the C-G cell; the latter was measured by using an iridium oxide/FTO electrode as the generator (*SI Appendix*, Fig. S5). The η of ss-DSSC/ALD/IrO$_x$ electrode is $44.3 \pm 6.5\%$. This value indicates that about half of the photocurrent arises from other sources, most likely oxidation of the hole-transport layer in an initial charging period.

The IPCE, which is an important parameter for photoelectrochemical cells, was also measured and is shown in Fig. 6. An IPCE value as high as 22% was observed at 540 nm, which is among the highest values yet reported for WS-DSPECs. The spectra closely overlap with the UV-vis absorption spectrum of the N3 dye on a nanocrystallineTiO$_2$ film electrode.

It is worth noting that the N3 dye molecule used in this study, with the Ru(III)/Ru(II) formal potential of 0.88 V vs. Ag/AgCl (32), is significantly less oxidizing than traditional light absorbers used for water oxidation. Sensitizers employed in WS-DSPECs
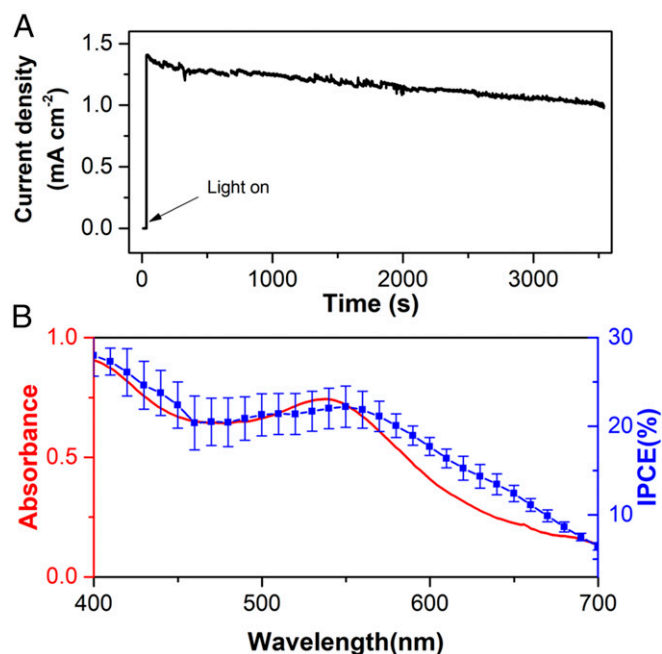

Fig. 6. (*A*) Chronoamperometry measurement of an ss-DSSC/ALD/IrO$_x$ photoelectrode for 1 h at an applied bias of 0.62 V vs. Ag/AgCl. Light source: 100-mW cm^{-2} xenon lamp with a 410-nm long-pass filter and an AM1.5 filter. (*B*) IPCE as a function of wavelength (blue) for an ss-DSSC/ALD/IrO$_x$ electrode at an applied bias of 0.62 V vs. Ag/AgCl. UV-vis absorption spectrum of N3 dye-sensitized TiO$_2$ electrode (red). Error bars indicate the SD based on the average of three measurements.

require careful design of their redox properties in the excited state, such as introducing electron-withdrawing groups in Ru-polypyridyl (33) and porphyrin sensitizers (34). The use of a buried junction bypasses this requirement by avoiding direct contact of the dye molecules with water. This in principle expands the gallery of sensitizers available for use in WS-DSPECs.

Conclusions

We have demonstrated that ss-DSSCs can be used in WS-DSPECs to decouple the light absorption and water-oxidation processes. A thin-film TiO$_2$ coating applied to the ss-DSSC by ALD effectively stabilizes the solar cell for operation in aqueous solution, although the performance of the cell in air is not as good because of increased series resistance at the TiO$_2$/hole-transport layer interface. Despite this performance loss, by electrodepositing an iridium oxide catalyst over the Au/TiO$_2$ layer, we realized a photocurrent density of 1.43 mA cm^{-2} at 1.23 V vs. reversible hydrogen electrode, with relatively good stability over 1 h. Faradaic efficiency determined by C-G method was 43% and an IPCE of 22% at 540 nm was measured. While the catalyst layer potential shifts slightly as the FTO potential changes (as in an adaptive junction), the potential profile under water-oxidation conditions is closely related to the current–voltage curve of the ss-DSSC, which suggests a buried photovoltaic junction. The fact that the potential drop occurs mostly within the ss-DSSC, rather than at the catalyst–electrolyte interface as expected from a buried junction, is due to the poor photodiode properties of the solar cell as indicated by its low fill factor. The buried junction design of ss-DSSCs adds to our understanding of SC-EC junction behaviors in the presence of a poor semiconducting material.

This cell design addresses an important stability issue in WS-DSPECs by physically separating the dye from the aqueous environment. Efficient charge separation in the ss-DSSC enables the ss-DSSC/ALD/IrO$_x$ electrode to oxidize water at a relatively

high photocurrent density. Further improvements are likely to be obtained by optimizing the ss-DSSC fabrication process to increase the fill factor, and by doping of the TiO_2 layer to lower the series resistance at the hole-conductor interface. We have also demonstrated that the buried junction approach enables the use of sensitizers with lower oxidizing power in WS-DSPECs, perhaps opening the door to use of sensitizers that more efficiently harvest sunlight.

1. Xu P, McCool NS, Mallouk TE (2017) Water splitting dye-sensitized solar cells. *Nano Today* 14:42–58.
2. Brennaman MK, et al. (2016) Finding the way to solar fuels with dye-sensitized photoelectrosynthesis cells. *J Am Chem Soc* 138:13085–13102.
3. Youngblood WJ, Lee SH, Maeda K, Mallouk TE (2009) Visible light water splitting using dye-sensitized oxide semiconductors. *Acc Chem Res* 42:1966–1973.
4. Gao Y, et al. (2013) Visible light driven water splitting in a molecular device with unprecedentedly high photocurrent density. *J Am Chem Soc* 135:4219–4222.
5. Lee SH, et al. (2012) Electron transfer kinetics in water splitting dye-sensitized solar cells based on core-shell oxide electrodes. *Faraday Discuss* 155:165–176, discussion 207–222.
6. Alibabaei L, Sherman BD, Norris MR, Brennaman MK, Meyer TJ (2015) Visible photoelectrochemical water splitting into H2 and O2 in a dye-sensitized photoelectrosynthesis cell. *Proc Natl Acad Sci USA* 112:5899–5902.
7. Wee K-R, et al. (2016) An aqueous, organic dye derivatized SnO_2/TiO_2 core/shell photoanode. *J Mater Chem A Mater Energy Sustain* 4:2969–2975.
8. Eberhart MS, et al. (2017) Water photo-oxidation initiated by surface-bound organic chromophores. *J Am Chem Soc* 139:16248–16255.
9. Li F, et al. (2015) Immobilizing Ru(Bda) catalyst on a photoanode via electrochemical polymerization for light-driven water splitting. *ACS Catal* 5:3786–3790.
10. Materna KL, Crabtree RH, Brudvig GW (2017) Anchoring groups for photocatalytic water oxidation on metal oxide surfaces. *Chem Soc Rev* 46:6099–6110.
11. Hanson K, et al. (2012) Photostability of phosphonate-derivatized, Ru(II) polypyridyl complexes on metal oxide surfaces. *ACS Appl Mater Interfaces* 4:1462–1469.
12. Xu P, Milstein TJ, Mallouk TE (2016) Flat-band potentials of molecularly thin metal oxide nanosheets. *ACS Appl Mater Interfaces* 8:11539–11547.
13. Hanson K, Losego MD, Kalanyan B, Parsons GN, Meyer TJ (2013) Stabilizing small molecules on metal oxide surfaces using atomic layer deposition. *Nano Lett* 13: 4802–4809.
14. Lapides AM, et al. (2015) Synthesis, characterization, and water oxidation by a molecular chromophore-catalyst assembly prepared by atomic layer deposition. The "mummy" strategy. *Chem Sci (Camb)* 6:6398–6406.
15. Zhang J, Freitag M, Hagfeldt A, Boschloo G (2018) Solid-state dye-sensitized solar cells. *Molecular Devices for Solar Energy Conversion and Storage* (Springer, Singapore), pp 151–185.
16. Bach U, et al. (1998) Solid-state dye-sensitized mesoporous TiO_2 solar cells with high photon-to-electron conversion efficiencies. *Nature* 395:583–585.
17. Xu T, Chen L, Guo Z, Ma T (2016) Strategic improvement of the long-term stability of perovskite materials and perovskite solar cells. *Phys Chem Chem Phys* 18: 27026–27050.
18. Hu S, et al. (2015) Thin-film materials for the protection of semiconducting photoelectrodes in solar-fuel generators. *J Phys Chem C* 119:24201–24228.
19. Chen YW, et al. (2011) Atomic layer-deposited tunnel oxide stabilizes silicon photoanodes for water oxidation. *Nat Mater* 10:539–544.
20. McCool NS, et al. (2016) Proton-induced trap states, injection and recombination dynamics in water-splitting dye-sensitized photoelectrochemical cells. *ACS Appl Mater Interfaces* 8:16727–16735.
21. Zhao Y, Vargas-Barbosa NM, Hernandez-Pagan EA, Mallouk TE (2011) Anodic deposition of colloidal iridium oxide thin films from hexahydroxyiridate(IV) solutions. *Small* 7:2087–2093.
22. Zhao Y, et al. (2015) Understanding the effect of monomeric iridium(III/IV) aquo complexes on the photoelectrochemistry of IrO(x)·nH2O-catalyzed water-splitting systems. *J Am Chem Soc* 137:8749–8757.
23. Sherman BD, Sheridan MV, Dares CJ, Meyer TJ (2016) Two electrode collector-generator method for the detection of electrochemically or photoelectrochemically produced O2. *Anal Chem* 88:7076–7082.
24. Swierk JR, et al. (2015) Metal-free organic sensitizers for use in water-splitting dye-sensitized photoelectrochemical cells. *Proc Natl Acad Sci USA* 112:1681–1686.
25. Cappel UB, Daeneke T, Bach U (2012) Oxygen-induced doping of spiro-MeOTAD in solid-state dye-sensitized solar cells and its impact on device performance. *Nano Lett* 12:4925–4931.
26. Grätzel M, et al. (1998) Solid-state dye-sensitized mesoporous TiO_2 solar cells with high photon-to-electron conversion efficiencies. *Nature* 395:583–585.
27. Burschka J, et al. (2011) Tris(2-(1H-pyrazol-1-yl)pyridine)cobalt(III) as p-type dopant for organic semiconductors and its application in highly efficient solid-state dye-sensitized solar cells. *J Am Chem Soc* 133:18042–18045.
28. Yagi M, Tomita E, Sakita S, Kuwabara T, Nagai K (2005) Self-assembly of active IrO2 colloid catalyst on an ITO electrode for efficient electrochemical water oxidation. *J Phys Chem B* 109:21489–21491.
29. Lin F, Boettcher SW (2014) Adaptive semiconductor/electrocatalyst junctions in water-splitting photoanodes. *Nat Mater* 13:81–86.
30. Lin F, Boettcher SW (2016) Advanced photoelectrochemical characterization: Principles and applications of dual-working-electrode photoelectrochemistry. *Photoelectrochemical Solar Fuel Production* (Springer International Publishing, Cham, Switzerland), pp 323–351.
31. Mills TJ, Lin F, Boettcher SW (2014) Theory and simulations of electrocatalyst-coated semiconductor electrodes for solar water splitting. *Phys Rev Lett* 112:148304.
32. Nazeeruddin MK, et al. (1993) Conversion of light to electricity by cis-X2bis(2,2′-bipyridyl-4,4′-dicarboxylate)ruthenium(II) charge-transfer sensitizers (X = Cl-, Br-, I-, CN-, and SCN-) on nanocrystalline titanium dioxide electrodes. *J Am Chem Soc* 115: 6382–6390.
33. Gillaizeau-Gauthier I, et al. (2001) Phosphonate-based bipyridine dyes for stable photovoltaic devices. *Inorg Chem* 40:6073–6079.
34. Materna KL, et al. (2017) Optimization of photoanodes for photocatalytic water oxidation by combining a heterogenized iridium water-oxidation catalyst with a high-potential porphyrin photosensitizer. *ChemSusChem* 10:4526–4534.